Meas. Sci. Technol. **20** (2009) 045403 (12pp) doi:10.1088/0957-0233/20/4/045403

A method for three-dimensional interfacial particle image velocimetry (3D-IPIV) of an air–water interface

Damon E Turney[1], **Angelika Anderer**[2] **and Sanjoy Banerjee**[3]

[1] Bren School of Environmental Science and Management, University of California, Santa Barbara, CA 93106, USA
[2] Technical University of Munich, Munich, Germany
[3] Department of Chemical Engineering, City College of New York, NY, USA

E-mail: dturney@bren.ucsb.edu

Received 1 October 2008, in final form 6 February 2009
Published 10 March 2009
Online at stacks.iop.org/MST/20/045403

Abstract
A new stereoscopic method for collecting particle image velocimetry (PIV) measurements within ∼1 mm of a wavy air–water interface with simultaneous measurements of the morphology of the interface is described. The method, termed three-dimensional interfacial particle image velocimetry (3D-IPIV), is tested in a wind wave channel with a wind speed of 5.8 m s^{-1}, water depth of 10 cm and a fetch of ∼9 m. Microscale breaking waves populate the interface and their flow patterns are clearly visible in the velocimetry results. The associated capillary waves and surface divergence patterns are observed. Several statistical measurements of the flow are compared with independent measurements and good agreement is found. The method shows great promise for investigating the transfer of momentum, heat and gases across an air–water interface, both in the laboratory and in field settings. Additional methods are described for manufacturing the flow tracers needed for the 3D-IPIV method. These tracers are likely to be useful for other researchers, and have the characteristics of being fluorescent, neutrally buoyant, non-toxic, monodisperse, inexpensive and easy to manufacture.

Keywords: PIV, particle image velocimetry, air water interface, wind waves, water waves, stereo PIV, laboratory channel

M This article features online multimedia enhancements

(Some figures in this article are in colour only in the electronic version)

1. Introduction

1.1. Overview

The transfers of momentum, heat and gases across air–water interfaces are important processes for many industrial and environmental systems. The published literature on the subject is extensive and dates back at least a hundred years. In spite of this, the transfer processes are far from being understood fully. For example, recent predictions of the global oceanic uptake of carbon dioxide, which are based on the best understandings of air–water gas transfer, give disagreement amongst each other of factors of up to 4 (Ho *et al* 2006, Donelan and Wanninkhof 2002). A similar uncertainty surrounds predictions for heat and momentum transfer, where progress has been made for open ocean conditions (Blanc 1985, Fairall *et al* 2003), but there still exists large uncertainty for coastal waters (Blanc 1985, Sopkin *et al* 2007) and inland waters (Webster *et al* 2003). Although these transfer processes are governed by known equations, e.g., the advection–diffusion equation or Navier–Stokes equations, an understanding of their physical workings remains elusive. This is because the details of how the velocity terms in these equations interact with the scalar terms, or with themselves, are not well understood. Additional complexities, such as effects from surfactants, put the processes into further uncertainty.

In the scientific literature, hypotheses have been made to describe the nature of the near-surface water motions that affect the transfers (Danckwerts 1951, Banerjee *et al* 1968, Fortescue and Pearson 1967, McCready 1986, Hunt and Graham 1978). Recent observations of these water flows have advanced the understanding (Brumley and Jirka 1987, Xu *et al* 2006, Turney *et al* 2005, Garbe *et al* 2004) and it appears that the most important water motions are those that occur within a few hundred microns of the interface. However, the technical difficulty of making measurements so close to a moving air–water interface has limited the number of reliable measurements reported in the literature, and there remains much uncertainty about the role of the near interfacial motions. In this paper we describe a new particle image velocimetry (PIV) method which accurately measures velocity fields on a three-dimensional moving air–water interface, within 1 mm of the interface, while simultaneously mapping the morphology of the interface. This method is termed three-dimensional interfacial particle image velocimetry (3D-IPIV). It is a promising new route to understanding the transfer of momentum, heat and gases across the air–water interface, and also for understanding the generation and dynamics of water waves. The method may easily be modified to operate closer than 1 mm from the interface.

During the development of this method a large number of $\sim$50 μm diameter fluorescent hydrophilic microspheres were required as flow tracers for the 3D-PIV technique. Specifically, three billion such microspheres were needed. On a limited budget this required that we invent new methods for cheaply producing such microspheres. We eventually succeeded in creating new methods for producing fluorescent, neutrally buoyant, hydrophilic microspheres from non-toxic compounds, using a safe, simple and inexpensive dispersion process. This paper also describes how to produce these microspheres.

1.2. Prior work on velocities near an air–water interface

Numerous techniques have been published in the literature for investigating the fluid motions near an air–water interface. For example, many researches have developed techniques for measuring the slope of the air–water interface (Lange *et al* 1982, Jahne *et al* 2005, Zappa *et al* 2008) or its three-dimensional shape (Tsubaki and Fujita 2005). Other researchers have focused on the velocities near the interface. These investigations will be reviewed in the following paragraphs. However, the technique developed by this paper is distinct. Here the specific need is for measurements of the topography of the air–water interface with simultaneous velocimetry measurements. An additional requirement is that the velocimetry results need to come from within $\sim$1 mm of the interface. Therefore we will only review prior methods for measuring velocities near an air–water interface. At least eight different techniques have been used in published studies for accomplishing this. The following section will summarize these techniques and at its end we will give the motivation for developing the new methods presented in this paper.

One of the first visualization techniques was to string a platinum wire taught near the interface and place a voltage difference on it relative to the water, so as to excite electrolysis and generate small hydrogen and oxygen bubbles (McLeish and Putland 1975, Okuda *et al* 1976, Rashidi and Banerjee 1990, Rashidi *et al* 1991). High-speed photography of the bubbles leads to velocity measurements through PIV calculations. These investigations occurred before the advent of digital cameras and therefore the velocities were usually determined by eye, i.e., using rulers and calculators. Several important conclusions resulted from these early studies, including a description of the transient evolution of the velocity boundary layer on a sheared interface (McLeish and Putland 1975), discovery of streaky and down-welling flows that also occur on a sheared interface (Rashidi and Banerjee 1990), descriptions of microscale breaking waves and capillary-gravity waves at higher wind speeds (Okuda *et al* 1976) and understandings of the characteristics of eddies from the channel bottom and their interaction with the interface and mass transfer rates (Rashidi *et al* 1991). However, this bubble technique has disappeared from use, largely due to the effect of the wire on the flow field and the difficulty of controlling the size and buoyancy of the bubbles (Banner and Peirson 1998).

Laser Doppler velocimetry (LDV) became available in the late 1970s and was applied to a non-sheared air–water interface in channel flow (Komori *et al* 1982, 1989, Nezu and Rodi 1986). These measurements confirmed the damping of the interface-normal velocities, and came to a useful conclusion establishing the relation between the frequency of large eddies impinging on the interface and interfacial mass transfer rates (Komori *et al* 1989). At about the same time LDV was applied to wind waves (Caulliez 1987, Melville and Rapp 1988, Cheung and Street 1988, Komori *et al* 1993). However, since LDV is a measurement that occurs at a single location, it cannot provide enough information on the patterns of velocity that are important for the interfacial transfers. Additionally, it is quite costly and since the mid-1990s researchers have turned to developing alternatives to LDV.

Another early technique was to use a split-film anemometer immersed in the water and held at a known distance from the interface. Some promising results were found with this method, notably that the statistical variance of the vertical and horizontal velocities agreed with the 'method of images' theory of Hunt and Graham (1978). However, the only known successful use of this technique was from Brumley and Jirka (1987) and it was never repeated. This is likely because the location of the split-film anemometer was difficult to control and also because the anemometer influenced the flow field.

Beginning in the 1990s and continuing to the present, researchers have favored visualization techniques wherein digital cameras capture images of flow tracers in the water. Velocities are calculated from these images via digital PIV. The most common such algorithm is to use cross-correlations of small sub-windows of the digital camera pictures, as described by Willert and Gharib (1991). Notable early applications of the technique to the air–water interface are Lin and Rockwell (1994) and Banner and Peirson (1998). When this technique is applied to the flow near the air–water interface, there seems to be as many experimental configurations as there

are researchers. The following paragraphs describe the most promising ones.

Many investigators have taken to sprinkling a powder of flow tracers on the air–water interface (Kumar *et al* 1998, Tamburrino and Gulliver 2002, 2007, Turney *et al* 2005, Tsumori and Sugihara 2007). A defining principle of this technique is that, due to buoyancy or surface tension, these flow tracers remain stuck on the air–water interface. The camera views down on these tracers from above the interface and PIV is performed on their movements. Unfortunately there are problems with the accuracy of this technique for the following reasons: (i) in regions where the interfacial velocity converges the flow tracers bump into one another, or as an alternative description the surface meniscus created by one tracer bumps into that created by neighboring tracers, consequently creating a 'jammed' mat of surface tracers which misrepresents the underlying fluid flow; (ii) these same jammed mats of surface particles slow down the water flow and therefore the technique becomes invasive; (iii) in regions where the interfacial velocity strongly diverges, the flow tracers move away leaving a blank spot and nothing remains for the PIV algorithm to operate with. Due to these problems of accuracy and invasiveness this technique will likely see less use in future measurements.

The laboratory of Khoo recently produced a promising solution to this problem, described in Law *et al* (1999) and used extensively in Law and Khoo (2002) and Xu *et al* (2006). They used a digital PIV method wherein one camera viewed the air–water interface from below the interface and a second camera viewed the same location from above the interface. They dispersed neutrally buoyant flow tracers throughout the water phase, i.e., the tracers were not stuck to the interface and therefore the 'jamming' problems did not arise. A vertical sheet of laser light illuminated the tracers, giving a side view of water motions. To accurately track the location and velocity of the interface they dissolved a fluorescent dye into the water, which was stimulated by the same laser light sheet used to illuminate the flow tracers, and viewed the scene with a second side-view camera located above the air–water interface. The second camera was able to accurately locate the air–water interface along its intersection with the laser light sheet. The technique resulted in beautiful confirmation of the predictions of Hunt and Graham (1978) for turbulence intensity near an interface (Law and Khoo 2002) and also gave nice empirical support for surface divergence theories of air–water gas transfer (Xu *et al* 2006). The success of this technique will probably continue in future investigations.

McKenna and McGillis (2004) also used a digital PIV approach for investigating surface divergence motions. They placed a single camera above the air–water interface pointing straight down. They seeded the water with neutrally buoyant acrylic microspheres impregnated with a fluorescent dye. A cone of laser light was shone down on the interface and into the water. To ensure their camera would only see particles near the interface they used a lens with a very slim range of focus. They state that the camera lens had a depth of focus of 5–10 mm (McKenna 2000), but the PIV results represent flows a bit closer than 5 mm. Their experiments found an interesting agreement between measured mass transfer rates and surface divergence theories. However, this method should be executed with a bit of caution since 5 mm is quite a large depth of view. Especially when surfactants are present, the water velocity at, say, 3 mm depth can be completely opposite from the interfacial velocity.

This concludes the listing of known published techniques for observing and measuring near-surface air–water flows. Note that the only accurate and reasonably non-invasive technique is that of Law *et al* (1999). This brings us to the motivation for the methods presented in this paper. First, the methods of Law *et al* give interfacial velocities along a line, i.e., along the intersection of the laser light sheet and the interface. It would be very informative to observe interfacial velocities along the plane of the air–water interface rather than just along a line. This would allow better information for understanding the Navier–Stokes and advection–diffusion equations. For example, analysis of these equations with a Lagrangian reference frame becomes possible. Second, since Law *et al* require that a camera and a laser lie in the water, it is difficult to transfer their methods to field settings, e.g., at ocean or on a lake. Third, it would be good to provide independent confirmation of the results found in Law and Khoo (2002) and Xu *et al* (2006).

1.3. Prior methods for manufacturing PIV flow tracers

As mentioned earlier, the PIV method described in this paper requires that the water phase be seeded with neutrally buoyant fluorescent microspheres. Adequate seeding for our experiments required three billion of these microspheres, each at $\sim$50 μm diameter. Purchasing these microspheres from a commercial vendor would have been exorbitantly costly and, in addition, we could not find a commercialized microsphere with the specifications needed for our new PIV method. Therefore we took up the task of developing our own manufacturing methods for microspheres with the following characteristics: (i) fluorescent with absorption of light in blue-green wavelengths and emission in red wavelengths, (ii) neutrally buoyant in water, (iii) diameters of $\sim$50 μm with deviations from this of less than 25%, (iv) hydrophilic so that they do not stick to the air–water interface, (v) sturdy enough to pass through the water pumps unharmed and (vi) cheap, easy and safe to manufacture at the rate of billions of microspheres per week.

Dozens of papers exist in the scientific literature or US patent archives describing techniques for manufacturing microspheres but none with the specifications we needed. The various existing techniques can be categorized by how the bulk chemicals are initially broken into microspheres. This can proceed through membrane-induced dispersions (Ma *et al* 1999, Sefton *et al* 1984), stirred dispersions (Giannola *et al* 1995), seed-swelling dispersion (Okubo *et al* 1991) or grinding (Pervez and Solomon 1994). Many of these dispersion techniques produce liquid microspheres that must be hardened. The hardening process can also be categorized as a polymerization reaction (Okubo *et al* 1991), a solvent evaporation process (Sefton *et al* 1984, Pradeesh *et al* 2005) or a phase-change process (Giannola *et al* 1995).

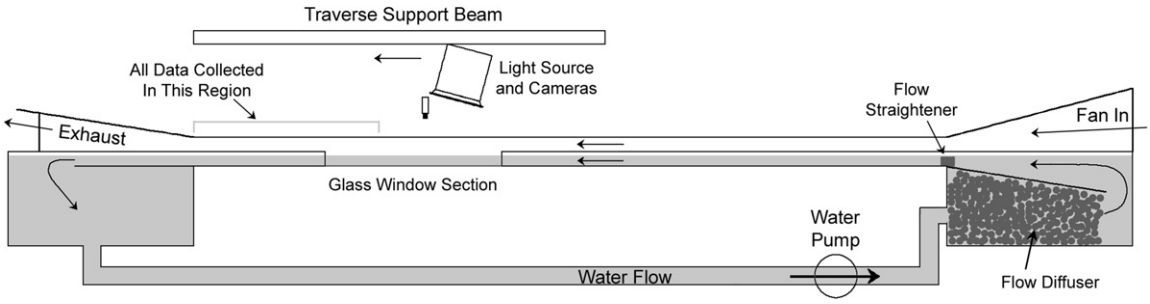

Figure 1. The wind wave channel in which the experiments were performed. The water level is denoted by the shade of gray. The top half of the channel was constructed of clear acrylic plastic. The bottom half was stainless steel. The large tanks were made of HDPE plastic. A glass window replaced this steel over a 1.7 m section of the channel, and allowed viewing of the flow from the sides and bottom. In the upstream tank a pile of random packing was placed for use in different experiments, not reported here, but this random packing acted coincidentally as a good flow diffuser.

We tried several unsuccessful methods for producing our desired microspheres, initially focusing on grinding techniques. A hydrophilic binder was mixed with fluorescent pigment. Hollow glass microballoons, of $\sim$18 μm diameter, were also added to control the density. The mixture was then dried, ground in a blender and then sieved to produce $\sim$75 μm microparticles. This method never produced satisfactory results because the grinding process compacted the hydrophilic binder and broke open the microballoons. Therefore the density of the resulting microparticles could never be controlled to better than $\pm$25%. Our focus then shifted to solvent evaporation emulsion techniques (Sefton *et al* 1984, Pradeesh *et al* 2005) whereby we dissolved ethylene vinyl acetate (EVA) in dichloromethane. Fluorescent pigment was also mixed in and we then emulsified the mixture in water. Poly-vinyl alcohol was used as a surfactant and a stabilizer. The dichloromethane slowly evaporates out of the emulsion resulting in hard EVA microspheres with the fluorescent pigment trapped inside. This technique worked very well, but scaling the process up to billions of microspheres would require tens of liters of dichloromethane. Releasing this much dichloromethane to the atmosphere via evaporation was undesirable from an environmental perspective.

We therefore shifted focus again to techniques that use only non-toxic materials. This led us to use the molten wax dispersion technique, which we successfully developed into the method used to make the flow tracers for all of the PIV measurements reported in this article. Three billion of these flow tracers were manufactured in a matter of weeks and at low cost. To develop this manufacturing method, much trial and error had to be done to find a surfactant that could keep the wax dispersion stable, especially during the phase transition when the wax becomes a polycrystalline solid. At this point the microspheres develop tiny spikes on their surface, which pierce the protective coating of surfactants (Golemanov *et al* 2006). Golemanov *et al* searched for and found surfactants that overcome this problem for low-melting point waxes. However, we needed to use high-melting point waxes, with melting points near 80 °C, and therefore the surfactants of Golemanov *et al* did not work. Numerous attempts resulted in a coagulated mess of wax microparticles. After a long search, we found a few surfactants that worked for high-melting point waxes such as paraffin wax, carnauba wax and beeswax. More details are given in the following sections.

2. Methodology

2.1. The wind wave channel

The experiments took place in a laboratory wind wave channel at the University of California at Santa Barbara, with the following dimensions: 12.0 m long, 0.70 m wide and 0.30 m tall. Figure 1 gives a graphical picture of the channel. Two large tanks, 2.0 m long $\times$ 1.0 m deep $\times$ 1.0 m wide, comprised the upstream and downstream ends of the channel. These tanks functioned to create smooth entrance and exit flows, and also to dampen waves. The light source, optical components and cameras were built onto a single assembly, which was mounted to a digitally controlled 4.3 m long traverse, i.e. a Parker Motion linear actuator model HPLA, driven by a stepper motor and belt. This traverse system allowed the 3D-IPIV assembly to move downstream at controlled steady speeds. The accuracy and consistency of the traverse speed was assured by the manufacturer, and additionally tested by our own stopwatch and PIV measurements. A flow straightener was placed at the upstream entrance of the channel. It consisted of an array of 15 cm long $\times$ 5 cm tall fins oriented along the direction of the flow. A surface skimmer operated at the downstream end of the channel to constantly filter surfactants off the air–water interface. This skimmed water was recirculated through filters back into the upstream tank. The channel water was potable tap water from the local municipality. The wave capacitance measurements took place just upstream from the downstream tank, at a fetch of 9.9 m. The Pitot tube anemometer measurements took place at a fetch of 9.6 m. All of the 3D-IPIV images were captured as the traverse moved the cameras downstream at a steady speed of 0.24 m s^{-1}. The cameras therefore collected images at fetches from 8.5 m to 9.9 m. All the measurements for this study occurred at fetches between 8.5 and 9.9 m.

2.2. The 3D-IPIV system

The core of the 3D-IPIV system was two digital cameras, mounted in a stereo configuration to an assembly that was

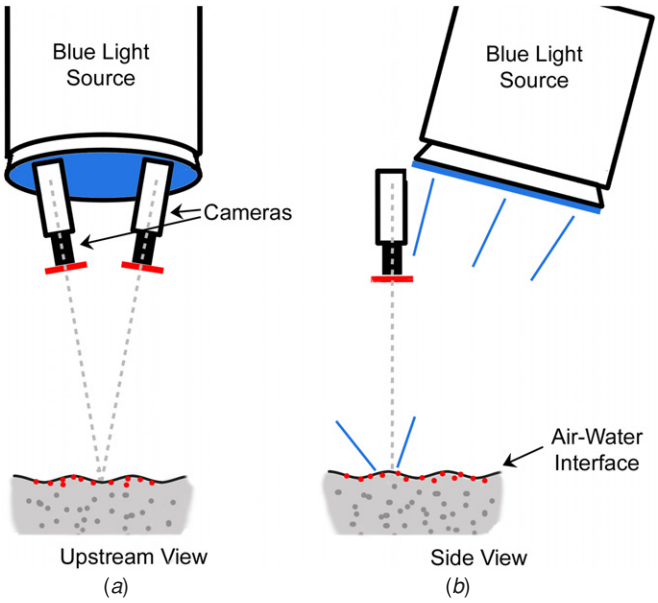

Figure 2. The new 3D-IPIV technique is shown from two angles: (*a*) the view is upstream; (*b*) the view is from the side as in figure 1. The water is dyed strongly black. The fluorescent microsphere flow tracers are seen to fluoresce red when they are near the air–water interface, but remain invisible when they are deeper than 1 mm in the water phase.

mounted to the traverse. A source of illumination was also mounted to this assembly. Figure 2 shows a graphical sketch of this assembly. The cameras were both Kodak Motion Corder SR models with 512 × 480 pixel resolution capable of full frame capture rates up to 250 frames s^{-1}. The cameras were made to capture synchronized image pairs by use of sync inputs and a signal from a function generator. The front optics of both cameras were 30 cm above the water surface and were angled at 10° with respect to gravity, i.e. 20° with respect to each other. The lenses were Navitar 17 mm $f/0.95$ models. The cameras viewed the same spot on the air–water interface, but from slightly different angles. The angle 20° was chosen due to the recommendations and analysis of Lawson and Wu (1997), who studied the error involved in the same camera configurations and stereoscopic calculations used here. Their results showed that 20° was an optimal configuration, and produced an error of 1% for displacements in the horizontal plane of the air–water interface and an error of 3% for displacements in the vertical direction. More information about the PIV and stereoscopic calculations will be given in section 2.5.

The water phase was seeded with fluorescent neutrally buoyant microspheres of diameter ∼42 μm. A bright blue light was shone on the air–water interface to stimulate the fluorescence of the microspheres. This blue light was hand built using a 1000 W Metal Halide Ushio blue aquarium bulb powered by a Lumalux 1000 W flicker-free electronic ballast. The bulb was housed in a movie-set aluminum HMI can with a silvered reflector on the backside and a 29 cm glass Fresnel lens on the front side to concentrate the light. Also on the front side of the light can were two 30 cm diameter red-blocking dichroic filters from High End Systems and one 30 cm diameter infrared-blocking dichroic filter from Deposition Sciences. These filters made the light into a very pure blue-green. Wavelengths greater than 550 nm were heavily suppressed. The resulting irradiance of the blue-green light on the air–water interface was measured at ∼500 W m^{-2}. This blue-green light stimulated the fluorescent microspheres in the water. The CCD cameras could easily see the fluorescing microspheres. The CCD cameras could not, however, see the reflections of the blue-green stimulation light because strong red filters, model Hoya Optics Sharp Cut R-60, were mounted on the front of the camera lenses. These filters absorbed light with wavelengths less than 600 nm. The microspheres fluoresced at wavelengths from ∼550 to ∼800 nm and therefore the Hoya red filter allowed the microspheres to be clearly visible to the cameras. The water was dyed black with 1 to 1000 parts Lochness SS non-toxic pond dye. The dye attenuated the blue-green stimulation light from penetrating deep into the water. It also absorbed the emission light from the fluorescing microspheres. The end result was that the dye limited the water depth at which the microspheres were visible to the cameras.

To quantify the depth at which microspheres were visible we glued microspheres to a ruler every half-millimeter. This ruler was then placed through the air–water interface at a 45° angle as shown in figure 3(*a*). The water depths of the microspheres increased by 0.35 mm increments, due to the 45° angle of the ruler. The 3D-IPIV system took photographs of this scene and the results were analyzed to determine the depth at which microspheres are invisible to the camera. Results from this experiment are shown in figures 3(*b*) and (*c*), where it is seen that microspheres disappear when they are greater than ∼1 mm below the water surface. This was a very believable result, since the water appeared extremely opaque to the naked eye. It is important to note that this ∼1 mm attenuation length can be strengthened or weakened in future experiments, simply by changing the concentration of the black dye.

The effect of the pond dye and microspheres on the surface tension of the water was analyzed with a Thermo Cahn Radian 300 Dynamic Contact Angle surface tensiometer. These measurements found values of 72.2 mN m^{-1} for deionized water, 71.6 mN m^{-1} for the local city water of Santa Barbara, CA, 72.3 nN m^{-1} for deionized water with 1 to 1000 parts Lochness dye mixed in, and 72.2 mN m^{-1} for deionized water with Lochness dye and microspheres. The nominal value for surface tension was ∼73 mN m^{-1} (Weast 1981). We therefore concluded that the Lochness SS pond dye and microspheres had a negligible effect on the dynamic surface tension of the air–water interface. An interesting note, however, is that dipping two fingers into the water lowered the surface tension to ∼50 mN m^{-1}. Obviously this is due to oils from the fingers spreading onto the air–water interface, and is an important note to remember for any researchers doing experiments with air–water interfaces. Also, if the microspheres were allowed to be hydrophobic and accumulate un-wetted on the air–water interface the surface tension would again drop to ∼50 mN m^{-1}. During our experiments, we continuously skimmed and vacuumed the air–water interface to remove surfactant and surfactant particles. We also took great care

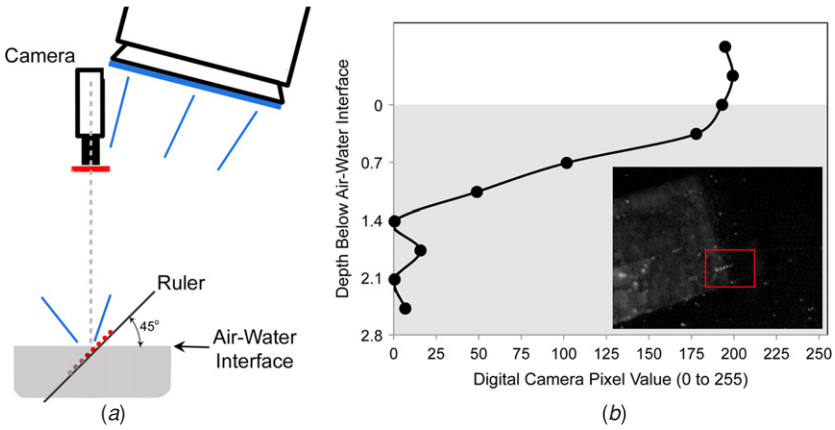

Figure 3. Measurements quantifying the attenuation of microsphere visibility in the dyed channel water. (*a*) The measurement method is shown graphically. (*b*) The brightness values of the microspheres are shown to decrease with depth and approach zero after ∼1 mm. (*c*) The raw camera image is shown, where the ruler descends into the water from the left and the glued microspheres are clustered close together in a short line, within the red rectangle.

to ensure that our microspheres were hydrophilic and would wet into the water easily rather than stick to the interface.

2.3. Preparation of the fluorescent microspheres

For preparation of the microspheres we procured 3 kg of paraffin wax granules with the melting point 70 to 80 °C, 2 kg of refined carnauba wax flakes, 250 g of Span 60 surfactant and 250 g of Span 20 surfactant, all from Sigma Aldrich. We also procured 4 L of sodium C14–16 olefin sulfonate from TheChemistryStore.com. The fluorescent pigment was UVHiVisOR orage-red pigment from LDP LLC.

The manufacturing of the microspheres used the following procedure: (i) prepare a 75 g molten mixture of paraffin wax and carnauba wax in a ratio that produces the desired microsphere density (the paraffin wax density was measured at 0.90 g ml^{-1}, the carnauba wax at 1.0 g ml^{-1} and the fluorescent pigment at 1.3 g ml^{-1}) which for our purposes was 1.0 g cm^{-3}; (ii) mix 45 g of fluorescent pigment into the molten wax mixture along with 0.5 g of Span 60 to stabilize the pigment within the wax environment; (iii) prepare a 4 L bath of water at temperature 95 °C; (iv) turn off the heat supply to the bath and begin mixing it with two industrial mixers or eggbeaters at ∼700 rpm; (v) within a few tens of seconds, pour the molten wax-pigment mixture into the stirred hot water bath; (vi) begin adding the sodium olefin sulfonate drop by drop to the hot bath and continue for a few minutes until 30 ml have been added, at which point the temperature of the water bath should have dropped to 75–80 °C and hundreds of millions liquid wax microspheres should have formed in the water bath dispersion; (vii) continue mixing the bath at ∼700 rpm until the temperature has dropped to 70 °C and the microspheres have turned solid; (viii) reduce the mixing speed to ∼300 rpm and add 30 ml of Span 20; (ix) continue to stir for 20 m.

This produced a dispersion of solid microspheres in the water bath. This dispersion then was poured through a sieve tower with a 75 μm sieve on the top, a 38 μm sieve in the middle and a 20 μm sieve at the bottom. The 38 μm sieve yielded microspheres with diameters between 30 and 75 μm. Yield was usually better than 75% by volume. The sizes of the microspheres could easily be modified by increasing or decreasing the stirring speed of the water bath, or by changing the amount of surfactant added to the water bath. The rejected microspheres were simply too small or too large. No microspheres or pigment particles fell through the smallest sieve. The rejected microspheres were re-melted and reprocessed. Therefore the only waste products of this entire process were the sodium olefin sulfonate, Span 60 and Span 20 dissolved in the water that fell through the lowest sieve. Note that these waste products are non-toxic. All microspheres in the sieves are washed with several liters of tap water to clean loose surfactants away. After this cleaning, the microspheres are ready for use in our PIV studies.

2.4. Flow conditions and application of the PIV system

A total of 6006 image pairs were captured by the 3D-IPIV system. Water depth was 0.10 m. A 375 W fan stood at the upstream end of the channel and forced wind down the airspace of the channel. Calibrated Pitot tubes and vane anemometers measured the wind speeds inside the channel from bottom to top, every 2 mm, except in regions obstructed by the wind waves. At the airspace centerline, the wind speed was 5.8 m s^{-1}. A few millimeters above the tallest waves it was 3.4 m s^{-1}. To prevent any return flows created by the wind wave drift current, the water in the channel was pumped in the downwind direction at a bulk velocity of 0.11 m s^{-1}. The experiments took place over a couple of weeks, but the water and air temperature never varied from 23 °C by more than a few °C. The Froude number was therefore ∼0.11 and the waves were entirely created by the wind shear, not by bottom-generated turbulence.

As mentioned previously, the cameras and the light source for the 3D-IPIV system were mounted on a traverse and moved at 0.24 m s^{-1} downstream. We took note of this speed and added it onto our PIV results so as to put our velocimetry results in the reference frame of a stationary laboratory observer. The main advantage of this traversing system was more accurate

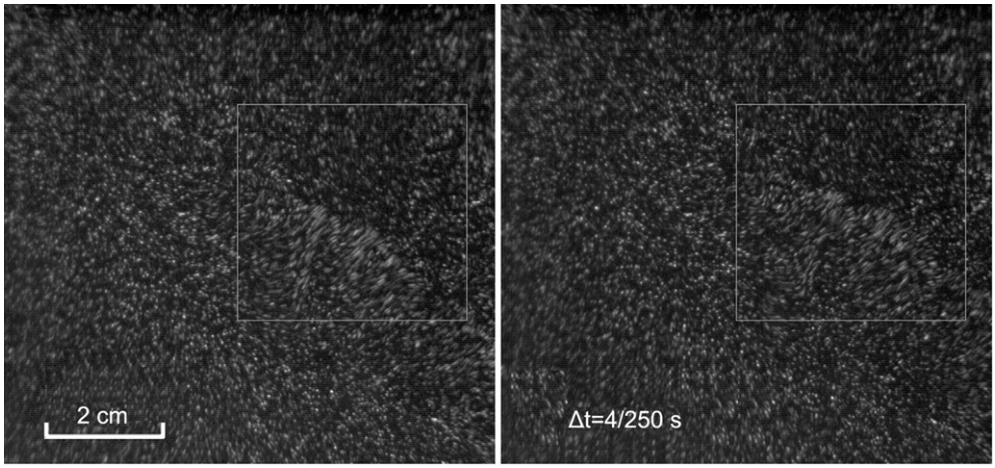

Figure 4. Raw images of the air–water interface from the left camera. The image on the right was taken 0.016 s after the image on the left. A wave is seen moving upward on the right-hand side of the images, inside the gray squares. A weakness of the present implementation is the streaking of the flow tracer images, observed near the crests of the waves in the figure above. This adversely affects the PIV results. However, it is a limitation of a hardware setup that can easily be remedied, either with the use of a higher speed camera or with the use of a pulsed illumination source.

PIV, since the flow tracers will not move as quickly in the camera reference frame. As mentioned in subsection 2.1 the cameras were mounted 0.30 m above the mean water surface. Images were captured at 250 fps in sequences of 546 images. Eleven such sequences were captured, making a total of 6006 images.

The water was seeded with microspheres at a density of ∼750 000 microspheres per liter. A total of three billion microspheres were dispersed in the wind wave channel. This huge density of microspheres was necessary to ensure that enough microspheres were constantly in the cameras' view. The view of the cameras was a roughly 7 × 7 cm patch of water that penetrated no further than ∼1 mm into the water, as described previously. Figure 4 shows two example raw images from the 3D-IPIV system.

2.5. PIV and stereoscopic calculations

The 3D-IPIV calculations were based on a digital two-dimensional cross-correlation PIV algorithm, as described in Willert and Gharib (1991). A hierarchical scheme was also used, the same as described in Roesgen and Totaro (1995). For each image pair this PIV algorithm was applied in two different ways: (i) using an image pair from the left camera with a small time gap between the images, which resulted in a field of velocity vectors, or (ii) using a stereo image pair, in which case the images were taken simultaneously and resulted in a field of displacement vectors between patches of interface in camera A's perspective and the same patches in camera B's perspective. Due to the stereoscopic geometry of our 3D-IPIV camera setup, these displacements depended uniquely on the elevations of the corresponding patch of the interface. Therefore, the displacements may serve as a map of the morphology of the air–water interface. All that is needed is a set of correlation coefficients to calibrate the displacement vectors into elevations. The method for doing this is described in detail in Lawson and Wu (1997), but is recapped in the following paragraph.

To calibrate the relationship between displacements and elevation of the interface we collected a training dataset. The air–water interface was set to 10 cm depth. The cameras were pointed at the same location on the interface, then rigidly secured in place, and then focused and never touched again. The air–water interface was then raised, by addition of water, to 12 cm height and allowed to become calm and flat. Photographs of this scene were taken. The air–water interface was then lowered to 11.5 cm and photographs were again taken. This was repeated down to 8.5 cm water depth. PIV was performed on the stereo image pairs from each water height. Cubic spline interpolations were then made, for each resulting node from the PIV results, between displacement and water height. This established a set of equations to convert between the two-dimensional PIV output and water height, one for each PIV node. These equations were called upon any time a stereo image pair, with unknown water topography, was processed into three dimensions.

Now, putting it all together, for the processing of a single time step from our collection of 6006 image pairs, the 3D-IPIV procedure was as follows: (i) apply the two-dimensional PIV algorithm to a chronologically sequential image pair, to determine the interfacial velocities as projected onto a flat plane; (ii) apply the same two-dimensional PIV algorithm to the stereo image pair and then use the correlations to calculate the water surface topography; (iii) correct the velocities from step (i) so that they correspond to the true water surface rather than a flat plane. Step (iii) involves a simple trigonometric calculation with the slope of the water surface.

A few more details of the PIV calculations deserve mention and will be given in the remainder of this section. For step (i) from the previous paragraph, the initial size of the subwindows was 20 × 20 pixels, and the final subwindow size, which defines how many vectors result per image pair, was 16 × 16 pixels. These subwindows overlapped each other by 50%. Therefore each image pair produced a 116 × 124 field of velocity vectors. Step (ii) used initial subwindow sizes

of 40 × 40, and final sizes of 20 × 20 with overlaps of 25%. This resulted in 46 × 50 fields of water height. The reason for the larger subwindow sizes for step (ii) was that the PIV code needed bigger subwindows to make high quality correlations from the stereo image pairs. The water height fields were interpolated so that their pixel resolution matched that of the velocity vectors, i.e. 116 × 124.

The CCD cameras recorded brightness as values between 0 and 255. However, some pixels displayed a systematic background value. These values ranged from 0 to about 15. To keep these systematic values from affecting the PIV process, the background of each CCD sensor was calculated and subtracted from all images taken from with that corresponding camera.

Two error-checking algorithms were run on all PIV results to identify outliers. First, the PIV program flagged a vector as error if the maximum correlation coefficient, for a given node, was below 0.6. This check was run after each correlation coefficient maximum was found. A second error-checking algorithm was run at the end of the PIV process, after the entire vector field had been generated. It compared each PIV vector to the mean of the entire field of vectors. If the individual vector was more than 5 standard deviations away from the mean then it was flagged as error. Additionally, each PIV vector was compared to the median of its neighboring 64 vectors, and if it was more than 3.5 standard deviations away it was flagged as error. This error checking program was essentially the same as that recommended by Westerweel (1994). The second error-checking algorithm identified less than 1% of the PIV vectors as error. The first error-checking algorithm identified less than 5% as error. The flagged vectors were interpolated with their neighbors at the end of the PIV process, after the entire vector field had been generated. The high quality of accuracy of the vectors was apparent by visual inspection between the raw movies and the vector fields.

A simple sub-pixel PIV algorithm was also used for all PIV calculations. This algorithm was run after the hierarchical PIV had finished. For every subwindow in image A, this algorithm interpolated it and also interpolated the corresponding subwindow in image B, i.e. the subwindow in image B that holds the same flow tracers. The algorithm then maximized the cross correlation of these interpolated subwindows. The PIV resolution was thereby increased by a factor of 5 in each dimension, or 25 in total. The quality of the PIV results made notable qualitative improvements with this subpixel PIV routine. No rigorous error analysis of the subpixel method was performed. However, the method is simple and obviously worked well in all our observations. Any error inherent in this method should not be limiting and it is beyond the purposes of this paper to investigate such errors. A better understood sub-pixel PIV algorithm may be used in future versions of 3D-IPIV.

As a final check on errors in the PIV code, synthetic image pairs were generated that had flow tracer fields with known displacements, i.e. known movements of the tracers between the two images. The PIV code showed ∼0% error for this check. A secondary final check was run in which the 3D-IPIV assembly was moved down the channel at a known speed. The air–water interface was kept calm and stationary. The PIV results agreed with the known traverse velocity to within 3% error. More confidence in the code was established when the wave height statistics and water velocity statistics were compared to independent measurements, e.g. from capacitance wire gauges or stopwatch timing of flow tracers. These comparisons are given in detail in the next section.

3. Results and discussion

3.1. 3D-IPIV results

Of the 6006 image pairs taken by the cameras, only 190 were processed with the 3D-IPIV method. The reason for this low number was the time necessary for processing. Processing a single image pair required ∼1.5 h on a 2.0 GHz CPU. We ran all calculations with MATLAB. Each of these image pairs resulted in a field of 116 × 124 velocity vectors and a matching field of water heights, covering a patch of the air–water interface roughly 7 × 7 cm. For brevity we will refer to a 116 × 124 set of data from a single image pair as a 'time slice' of 3D-IPIV data.

Of the 190 time slices of data, 50 were spaced randomly in time so as to form a dataset for statistical calculations. The statistical calculations made from this dataset were average downwind velocity, rms downwind velocity, maximum and minimum downwind velocity, maximum and minimum wave height, surge height and rms water height. Since the dataset contained spatial and temporal dimensions, the statistical results were from ensembles over both space and time. Convergence of these statistical results was investigated by noticing the change in the statistical values as additional time slices were added to the dataset. The convergence of the statistical values was always within 10% of the mean value. For calculations of maximum and minimum, the distribution of values was observed to make sure the final answer was not an outlier, which was never the case. Therefore, we concluded that 50 time slices contained a sufficient amount of data to obtain reasonably accurate statistical results. These results are as follows. The average water height rose by 0.16 cm due to the wind pushing the water to the far end of the wind wave channel, which we call the 'surge height'. The standard deviation of water height was 0.36 cm. The tallest observed wave stood 1.12 cm above the average water height. The lowest trough was 0.83 cm below the average water height. The maximum and minimum recorded velocities in the downstream direction were 79.8 cm s^{-1} and −2.7 cm s^{-1}, respectively. The standard deviation of downstream velocity was 11.0 cm s^{-1} and the wind drift velocity was 22.5 cm s^{-1}.

The other 140 time slices were chronologically sequential, and therefore could be made into a three-dimensional movie of the flow of the air–water interface. A clip of this movie has been submitted to this journal's online repository. The images in figure 5 come from the middle of this movie, and correspond spatially and temporally to the small rectangles in the raw images in figure 4.

The water surface topography shows a notable change in water height at the location of the breaking wave front,

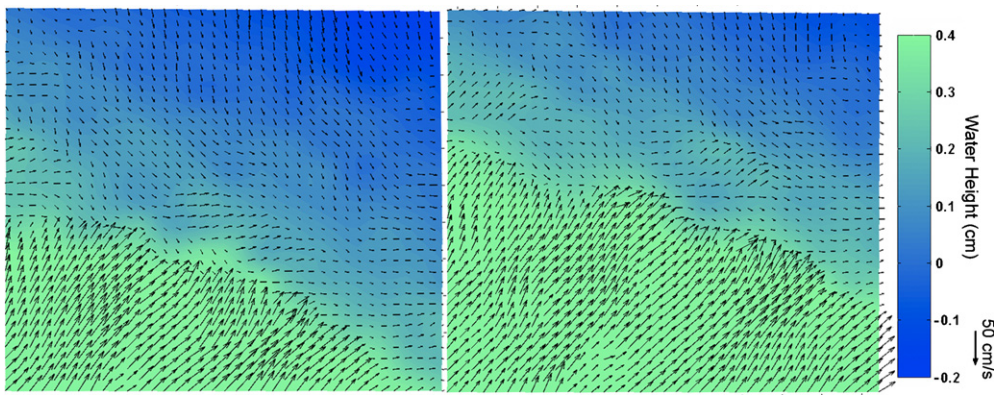

Figure 5. Results from the 3D-IPIV method for two time slices. The image on the right was collected 0.016 s after the image on the left. The velocity vectors are corrected so as to correspond to a contorted surface. The color scale on the right gives the height of the air–water surface relative to the mean height. The 50 cm s^{-1} vector on the right gives the scale for the velocity vectors. A microscale breaking wave is seen moving up and to the right. Capillary waves populate the face of the wave.

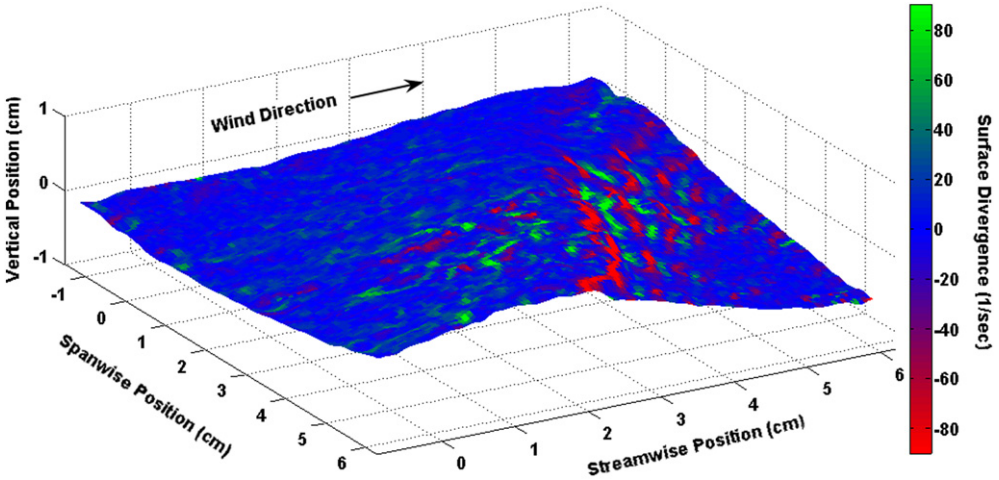

Figure 6. A three-dimensional image of surface divergence on a microscale breaking wave. Upwelling is seen behind the wave. Bands of alternating convergence and divergence are seen on the face of the wave, due to capillary waves and also due to the spilling region of the breaking wave.

and smaller capillary waves are seen in front of the breaking wave. This wave is a classic microscale breaking wind wave. Figure 6 shows a three-dimensional plot of the data from the left time slice of figure 5, except that figure 6 has not been zoomed in. Velocity vectors are not plotted in figure 6, but rather, the divergence of velocity vectors. This shows the breaking front of the wave as a zone of high convergence. Behind the breaking wave divergence is occurring more strongly, which corresponds to upwellings. In front of the breaking wave one can see several bands of convergence and divergence, which correspond to several capillary waves on the face of the wave. The divergence of surface velocity has recently received much attention for its role in mediating the transfer of gases at air–water interfaces (McKenna and McGillis 2004, Xu *et al* 2006, Turney *et al* 2005; Banerjee *et al* 2004).

3.2. Error analysis

The 3D-IPIV method described by this paper is simply the conglomerate of the standard PIV algorithm described in references such as Willert and Gharib (1991) or Roesgen and Totaro (1995), with the stereoscopic algorithms described by Lawson and Wu (1997). Errors for these methods have been well studied and are always ∼5% or less. The novelty of this current study does not come from the PIV algorithm, or the stereoscopic algorithm, but from the simultaneous use of stereoscopy and PIV, and also from the dyed black water, colored light source and color filters. Confidence in the accuracy of the 3D-IPIV method is here established by comparing the statistical results given in section 3.1 with independent measurements of the same statistics. These comparisons are given below.

The wire capacitance wave gauge recorded the surge height as 0.16 cm, the standard deviation of water level as 0.38 cm, the tallest wave as 1.03 cm and the lowest trough as −0.78 cm. A third measure of the maximum wave height was made during our Pitot tube measurements of wind speed. We could not place the Pitot tube within 1.1 cm of the interface without it being struck by a large wave. Mean surface drift velocity in the downwind direction was also measured by stopwatch timing the travel of floating particles, which is an

Table 1. Comparison of independent measurements of the wind waves to measurements from the 3D-IPIV method. Standard deviation is denoted by σ.

	Surge height (cm)	Water height σ (cm)	Tallest wave (cm)	Lowest trough (cm)	Mean downstream velocity (cm s^{-1})
3D-IPIV	0.16	0.36	1.12	−0.83	22.5
Wire gauge	0.16	0.38	1.03	−0.78	–
Pitot tube	–	–	1.1	–	–
Drifters	–	–	–	–	24.8

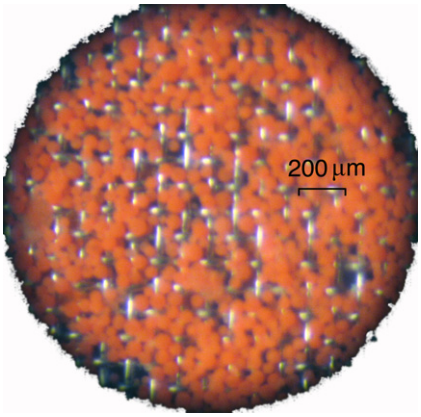

Figure 7. The fluorescent microspheres lying on a sieve with 38 μm openings.

established practice for measuring drift velocities, resulted in a drift velocity measurement of 24.8 cm s^{-1}. Table 1 compares these independent measurements to the 3D-IPIV results and to the Pitot tube observation. The independent measurements show consistent agreement to the 3D-IPIV results to within 10% error. Therefore, the 3D-IPIV method passes many tests for accuracy. Further, the three-dimensional shape of the wind waves shown in figure 6 qualitatively matches that reported in other investigations, for example figure 2 of Banner and Pierson (1998).

3.3. Microsphere results

In total we made approximately three billion microspheres of the desired specifications. The effort took about two weeks and cost only a few hundred US dollars, not including the research and development that went into discovering the manufacturing process. The microspheres were dumped into the water channel and allowed a day to distribute and fully wet their surfaces. As seen from figures 4 through 6 the microspheres worked very well as flow tracers for our new PIV method.

The distribution of diameters for the microspheres was measured on a Malvern Instruments Mastersizer. This showed that the sieved microspheres had a Gaussian size distribution with a mean diameter of 42 μm and a standard deviation of 10 μm. The non-sieved microspheres had a size distribution that was Gaussian except for a slight skewness toward larger sizes, i.e., skewness of ∼0.5, and had a mean diameter of 58 μm and a standard deviation of 16 μm. Figure 7 shows a random sample of the microspheres lying on a sieve with 38 μm openings. The sphericity of the microspheres was observed by a microscope to be excellent.

During research and development of our manufacturing methods we tested many surfactants and many materials for comprising the microspheres. The vast majority of these combinations failed to produce viable microspheres. In the cases where we used wax dispersions this was almost always because the solidification would cause the agglomeration of the microspheres into ∼5 mm clods. This problem was well documented by Golemanov *et al* (2006) who showed that crystallization of the wax resulted in small spikes on the microsphere surface that could penetrate any surfactant coatings. They also found that the quality of a surfactant choice could be quantified as a 'critical osmotic pressure' between two microspheres. Above this pressure the microspheres would agglomerate and below this pressure they would stay separate and viable. Golemanov *et al* found surfactants that worked well for low-melting point paraffins, such as tetradecane or hexadecane, which are liquid at room temperature. They found critical osmotic pressures that were on the order of 1 to 100 kPa (for the successful surfactants). For our purposes we needed a high-melting point wax and the surfactants from Golemanov *et al* did not work. However we discovered that sodium C14-16 olefin sulfonate did work well and we were able to use it produce microspheres as described in section 2. However the critical osmotic pressure we found was very low, near 0.01 kPa. Therefore this surfactant was not excellent in its ability to guard against agglomeration, but it was the best of the dozen or so surfactants we tried and it worked in our manufacturing process.

4. Conclusion

A novel method has been developed for gathering three-dimensional interfacial particle image velocimetry (3D-IPIV) from the plane of a wavy air–water interface. The velocities are guaranteed to be from a region within 1 mm of the interface. The method is reasonably non-intrusive and may hypothetically be transferred to a field setting without modification. The output of the method, for an instant in time, is a map of the elevation of the air–water interface and also the velocity vectors along that surface. The method was applied to a wind wave flow in a 12 m long channel with water depth of 10 cm, wind speeds of 5.8 m s^{-1} and fetch of ∼9 m. Microscale breaking waves were observed and the capillary waves on the wave faces were clearly visible. Upwellings behind the waves were also clearly visible. Statistical measurements of water

height and wave velocity were found to agree with independent measurements to within 10% error. The method shows great promise for the improved investigation of the transfer of momentum, heat and gases across air–water interfaces. The output from the method allows Lagrangian analysis of the governing equations for the transfer processes, which has not been possible with previous methods.

Also, a new method for manufacturing microspheres was invented. The size and density of the microspheres may be controlled, as well as the color and surface hydrophillicity. Fluorescent microspheres of 1.0 g cm^{-3} and size 42 μm were made for these experiments with good homogeneity. The manufacturing process was safe and simple, with high yield and almost no waste products. The microspheres themselves were composed of only non-toxic ingredients and hypothetically could be used in field settings.

Acknowledgment

The authors gratefully acknowledge the financial support from the NSF in the form of grant CTS-0553333.

References

Banerjee S, Lakehal D and Fulgosi M 2004 Surface divergence models for scalar exchange between turbulent streams *Int. J. Multiph. Flow* **30** 963–77

Banerjee S, Scott D S and Rhodes E 1968 Mass transfer to falling wavy liquid films in turbulent flow *Ind. Eng. Chem. Fundam.* **7** 22–7

Banner M L and Peirson W L 1998 Tangential stress beneath wind-driven air–water interfaces *J. Fluid Mech.* **364** 115–45

Blanc T V 1985 Variation of bulk-derived surface flux, stability, and roughness results due to the use of different transfer-coefficient schemes *J. Phys. Oceanogr.* **15** 650–69

Brumley B H and Jirka G H 1987 Near-surface turbulence in a grid-stirred tank *J. Fluid Mech.* **183** 235–63

Caulliez G 1987 Measuring the wind-induced water-surface flow by laser Doppler velocimetry *Exp. Fluids* **5** 145–53

Cheung T K and Street R L 1988 The turbulent layer in the water at an air–water interface *J. Fluid Mech.* **194** 133–50

Danckwerts P V 1951 Significance of liquid-film coefficients in gas absorption *Ind. Eng. Chem.* **43** 1460–7

Donelan M A and Wanninkhof R H 2002 *Gas Transfer At Water Surfaces* ed M A Donelan *et al* (Washington, DC: American Geophysical Union) pp 1–10

Fairall C W, Bradley E F, Hare J E, Grachev A A and Edson J B 2003 Bulk parameterization of air-sea fluxes: updates and verification for the COARE algorithm *J. Clim.* **16** 571–91

Fortescue G and Pearson J R A 1967 On gas absorption into a turbulent liquid *Chem. Eng. Sci.* **22** 1163–76

Garbe C S, Schimpf U and Jahne B 2004 A surface renewal model to analyze infrared image sequences of the ocean surface for the study of air–sea heat and gas exchange *J. Geophys. Res.* 109

Giannola L I, Decaro V and Severino A 1995 Carnauba wax microspheres loaded with valproic acid—preparation and evaluation of drug-release *Drug Dev. Ind. Pharm.* **21** 1563–72

Golemanov K, Tcholakova S, Denkov N D and Gurkov T 2006 Selection of surfactants for stable paraffin-in-water dispersions, undergoing solid-liquid transition of the dispersed particles *Langmuir* **22** 3560

Ho D T, Law C S, Smith M J, Schlosser P, Harvey M and Hill P 2006 Measurements of air–sea gas exchange at high wind speeds in the southern ocean: implications for global parameterizations (vol 33, art no L16611, 2006) *Geophys. Res. Lett.* **33** 321–7

Hunt J C R and Graham J M R 1978 Free-stream turbulence near plane boundaries *J. Fluid Mech.* **84** 209–35

Jahne B, Schmidt M and Rocholz R 2005 Combined optical slope/height measurements of short wind waves: principle and calibration *Meas. Sci. Technol.* **16** 1937–44

Komori S, Murakami Y and Ueda H 1989 The relationship between surface renewal and bursting motions in an open-channel flow *J. Fluid Mech.* **203** 103

Komori S, Nagaosa R and Murukami Y 1993 Turbulence structure and mass transfer across a sheared air–water interface in wind-driven turbulence *J. Fluid Mech.* **249** 161–83

Komori S, Ueda H, Ogino F and Mizushina T 1982 Turbulence structure and transport mechanism at the free-surface in an open channel flow *Int. J. Heat Mass Transfer.* **25** 513–21

Kumar S, Gupta R and Banerjee S 1998 An experimental investigation of the characteristics of free-surface turbulence in channel flow *Phys. Fluids* **10** 437–56

Lange P A, Jahne B, Tschiersch J and Ilmberger I 1982 Comparison between an amplitude-measuring wire and a slope-measuring laser water-wave gauge *Instrum. Rev. Sci.* **53** 651–5

Law C N S and Khoo B C 2002 Transport across a turbulent air–water interface *AIChE J.* **48** 1856–68

Law C N S, Khoo B C and Chew T C 1999 Turbulence structure in the immediate vicinity of the shear-free air–water interface induced by a deeply submerged jet *Exp. Fluids* **27** 321–31

Lawson N J and Wu J 1997 Three-dimensional particle image velocimetry: experimental error analysis of a digital angular stereoscopic system *Meas. Sci. Technol.* **8** 1455–64

Lin J C and Rockwell D 1994 Cinematographic system for high-image-density particle image velocimetry *Exp. Fluids* **17** 110–8

Ma G H, Nagai M and Omi S 1999 Study on preparation and morphology of uniform artificial polystyrene-poly(methyl methacrylate) composite microspheres by employing the SPG (Shirasu Porous Glass) membrane emulsification technique *J. Colloid Interface Sci.* **214** 264–82

McCready M J 1986 Spectral behavior of capillary waves in gas-liquid flows *Phys. Fluids* **29** 2836–42

McKenna S P 2000 Free-surface turbulence and air–water gas exchange *PhD Dissertation* Department of Ocean Engineering, Massacheusetts Institute of Technology, Boston

McKenna S P and McGillis W R 2004 The role of free-surface turbulence and surfactants in air–water gas transfer *Int. J. Heat Mass Transfer* **47** 539–53

McLeish W and Putland G E 1975 Measurements of wind-driven flow profiles in top millimeter of water *J. Phys. Oceanogr.* **5** 516–8

Melville W K and Rapp R J 1988 The surface velocity-field in steep and breaking waves *J. Fluid Mech.* **189** 1–22

Nezu I and Rodi W 1986 Open-channel flow measurements with a laser doppler anemometer *J. Hydraul. Eng., ASCE* **112** 335–55

Okubo M, Shiozaki M, Tsujihiro M and Tsukuda Y 1991 Studies on Suspension and Emulsion.122. Preparation of micron-size monodisperse polymer particles by seeded polymerization utilizing the dynamic monomer swelling method *Colloid Polym. Sci.* **269** 222–6

Okuda K, Kawai S, Tokuda M and Toba Y 1976 Detailed observations of the wind exerted surface flow by use of flow visualization method *J. Oceanogr. Soc. Japan* **32** 53–64

Pervez M S and Solomon T H 1994 Long-term tracking of neutrally buoyant tracer particles in 2-dimensional fluid-flows *Exp. Fluids* **17** 135–40

Pradeesh T S, Sunny M C, Varma H K and Ramesh P 2005 Preparation of microstructured hydroxyapatite microspheres using oil in water emulsions *Bull. Mater. Sci.* **28** 383–90

Rashidi M and Banerjee S 1990 The effect of boundary-conditions and shear rate on streak formation and breakdown in turbulent channel flows *Phys. Fluids* A **2** 1827–38

Rashidi M, Hetsroni G and Banerjee S 1991 Mechanisms of heat and mass-transport at gas-liquid interfaces *Int. J. Heat Mass Trans.* **34** 1799–810

Roesgen T and Totaro R 1995 2-Dimensional online particle imaging velocimetry *Exp. Fluids* **19** 188–93

Sefton M V, Brown L R and Langer R S 1984 Ethylene vinyl-acetate copolymer microspheres for controlled release of macromolecules *J. Pharm. Sci.* **73** 1859–61

Sopkin K, Mizak C, Gilberta S, Subramanian V, Luther M and Poor N 2007 Modeling air/sea flux parameters in a coastal area: a comparative study of results from the TOGA COARE model and the NOAA Buoy model *Atmos. Environ.* **41** 4291–303

Tamburrino A and Gulliver J S 2002 Free-surface turbulence and mass transfer in a channel flow *AIChE J.* **48** 2732–43

Tamburrino A and Gulliver J S 2007 Free-surface visualization of streamwise vortices in a channel flow *Water Resour. Res.* **43** W11410

Tsubaki R and Fujita I 2005 Stereoscopic measurement of a fluctuating free surface with discontinuities *Meas. Sci. Technol.* **16** 1894–902

Tsumori H and Sugihara Y 2007 Length scales of motions that control air–water gas transfer in grid-stirred turbulence *J. Marine. Syst.* **66** 6–18

Turney D E, Smith W C and Banerjee S 2005 A measure of near-surface fluid motions that predicts air–water gas transfer in a wide range of conditions *Geophys. Res. Lett.* **32** L04607

Weast R C (ed) 1981 *Handbook of Chemistry and Physics* (Boca Raton, FL: CRC Press) p F-45

Webster J R *et al* 2003 Factors affecting ammonium uptake in streams—an inter-biome perspective *Freshwater Biol.* **48** 1329–52

Westerweel J 1994 Efficient detection of spurious vectors in particle image velocimetry data *Exp. Fluids* **16** 236–47

Willert C E and Gharib M 1991 Digital particle image velocimetry *Exp. Fluids* **10** 181–93

Xu Z F, Khoo B C and Carpenter K 2006 Mass transfer across the turbulent gas-water interface *AIChE J.* **52** 3363–74

Zappa C J, Banner M L, Schultz H, Corrada-Emmanuel A, Wolff L B and Yalcin J 2008 Retrieval of short ocean wave slope using polarimetric imaging *Meas. Sci. Technol.* **19** 055503